Wake Development in Floating Wind Turbines: New Insights and Open Dataset from Wind Tunnel Experiments

Alessandro Fontanella[1], Alberto Fusetti[2], Stefano Cioni[3], Francesco Papi[3], Sara Muggiasca[1], Giacomo Persico[2], Vincenzo Dossena[2], Alessandro Bianchini[3], and Marco Belloli[1]

[1]Department of Mechanical Engineering, Politecnico di Milano, via La Masa 1, 20156 Milano, Italy.
[2]Department of Energy, Politecnico di Milano, Via Lambruschini 4, 20156 Milano, Italy.
[3]Department of Industrial Engineering, Università degli Studi di Firenze, Via di Santa Marta 3, 50139 Firenze, Italy.

Correspondence: Alessandro Fontanella (alessandro.fontanella@polimi.it)

Abstract. Floating offshore wind turbines represent a promising new technology in offshore renewables, but they are still in their early stages with few prototypes and limited performance data. As part of the NETTUNO research project, this study examines how platform movement affects the aerodynamics of a floating wind turbine rotor and connects its load response to the evolution of its wake. Wind tunnel experiments were performed on a 1:75 scale model wind turbine subjected to platform

5 movements in various directions. Collected data includes measurements of rotor loads and wind speed in the wake of the wind turbine at different downstream distances from the rotor. The study provides a detailed analysis of a selected portion of the data, while the entire dataset is accessible via an open repository. Results indicate that surge and pitch motions induce periodic thrust fluctuations, leading to variations in near wake velocity that peak at a reduced frequency of 0.6. Yaw motion causes oscillations in the yaw moment and lateral wake meandering. Combined surge and sway motions result in skewed apparent wind speed,

10 causing both wake velocity fluctuations and lateral meandering. Increased turbulence intensity near the wake center suggests enhanced wake mixing and potentially a faster recovery beyond a distance of 5 diameters downstream. New experimental data may serve as a foundation for validating numerical simulation tools, while the main findings of the study are thought to provide valuable knowledge for optimizing future large-scale floating wind farms.

1 Introduction

15 Floating wind power is the technology that can open the doors of deep-water sites to wind energy projects. Currently, the technology remains in what is often referred to as a pre-commercial stage (Barter et al., 2020). Existing pilot floating wind plants have project sizes of 10-50 MW. However, upcoming projects are significantly larger and will include from tens to hundreds of wind turbines, reaching gigawatt scale. On that scale, wind turbines in the farm are going interact through wakes–areas behind rotors with lower energy and higher turbulence compared to free-stream wind (Meyers et al., 2022). To date, research

20 on floating wind power has mostly focused on individual turbines, but upcoming projects raise concerns about wakes and aerodynamic interactions in large floating wind farms. Unlike bottom-fixed turbines, floating turbines may experience significant movements that impact rotor aerodynamics and wake formation. Moreover, full-scale measurements of floating wind turbine

1

wakes are scarce. Very recently, Özinan et al. (2024) studied the near wake of a 2 MW floating wind turbine and found no evident impact of wave-induced motions on the average velocity of the wake, partially contrasting theoretical speculations.

25 The effects of platform motion on the wake have been studied so far through wind tunnel experiments with model turbines and porous disk. Bayati et al. (2017a) examined the effect of surge motion on the near wake of a 1:75 scale model of a 10 MW wind turbine and discovered that the wake has wind speed fluctuations due to motion. Fontanella et al. (2021) expanded the experiment to include more surge motion conditions and described how motion influences the formation of tip vortices near the rotor. Fontanella et al. (2022a) carried out an experiment with a 1:100 scale model of a 15 MW turbine, which was subjected

30 to platform movements in different directions. They found that the average velocity and turbulence in the near wake were marginally lower with motion compared to the fixed case. (Messmer et al., 2024a) experimentally investigated the wake of a floating wind turbine experiencing harmonic sway and surge movements in a wind tunnel with laminar inflow conditions. They found that sway movements cause wake meandering, while surge movements create a pulsing wake, and both types of motion improve wake mixing. (Messmer et al., 2024b) studied in the wind tunnel the wake of a scale model wind turbine subjected

35 to surge motion with inflow turbulence intensity up to 3%. They found that as turbulence in the incoming wind increases, the wake recovery is less influenced by platform motion.

Porous disks have been utilized to investigate the wakes of floating wind turbines within atmospheric boundary layer flows. Schliffke et al. (2020) found that at 4.6 rotor diameters downstream, surge motion does not alter wake mean velocity, but it does affect turbulence intensity and turbulent kinetic energy profiles. Schliffke et al. (2024) demonstrated that harmonic platform

40 motion produces distinct frequency signatures in the far wake spectra, whereas broadband motion leaves no easily discernible marks.

The impact of platform motions in various directions on the wake of a floating wind turbine remains uncertain, and the interaction of wakes among floating wind turbines is yet to be studied. The NETTUNO project (Nettuno, 2023) aims to combine wind tunnel experiments with multi-fidelity simulations to get a better understanding of wake-turbine interactions

45 in floating wind turbines. This project phase explores how large movements affect wake development. The second phase will examine the interaction between two floating wind turbines caused by wakes.

The unique aspect of the experiment presented in this article is twofold: first, it investigates how platform movements, common to floating wind turbines and taking place in various directions, impact rotor aerodynamics; then, it connects the rotor response to wake development with an unprecedented level of detail. To this end, we measured both rotor loads and the wake of

50 a scaled-down wind turbine subjected to harmonic platform movements. Insights into wake evolution from the experiment can be utilized to optimize wind farm layouts, design floaters, and enhance control strategies at both the turbine and farm levels. Collected measurement data are accessible to the community and serve as a foundation for validating numerical simulation tools.

The paper is organized as follows. Section 2 presents the setup used for carrying out the wind tunnel experiment, which

55 includes the wind turbine scale model and the measurements taken in the test campaign. Section 3 describes the test scenarios. Section 4 explains the processing that was applied to measurement data collected in the experiment. Key results are discussed in Sect. 5. Section 6 draws the conclusions and proposes suggestions for future work.

2 Wind tunnel experimental setup

The experimental campaign was conducted in the atmospheric-boundary layer test section of Politecnico di Milano wind tunnel, which is $13.84\,\mathrm{m}$ wide by $3.84\,\mathrm{m}$ high by $35\,\mathrm{m}$ long. The test turbine, shown in Fig. 1, has a rotor diameter (D) of $2.38\,\mathrm{m}$ and it is mounted on a six-degrees-of-freedom robotic platform that mimics the rigid-body motions of floating foundations. This setup has been used in various experiments about the aerodynamics of floating wind turbines and the data from this turbine, collected in earlier projects (Fontanella et al., 2021), were recently utilized in the International Energy Agency Task 30 to verify the accuracy of predicted aerodynamic loads by various offshore wind modeling tools (Bergua et al., 2023; Cioni et al., 2023).
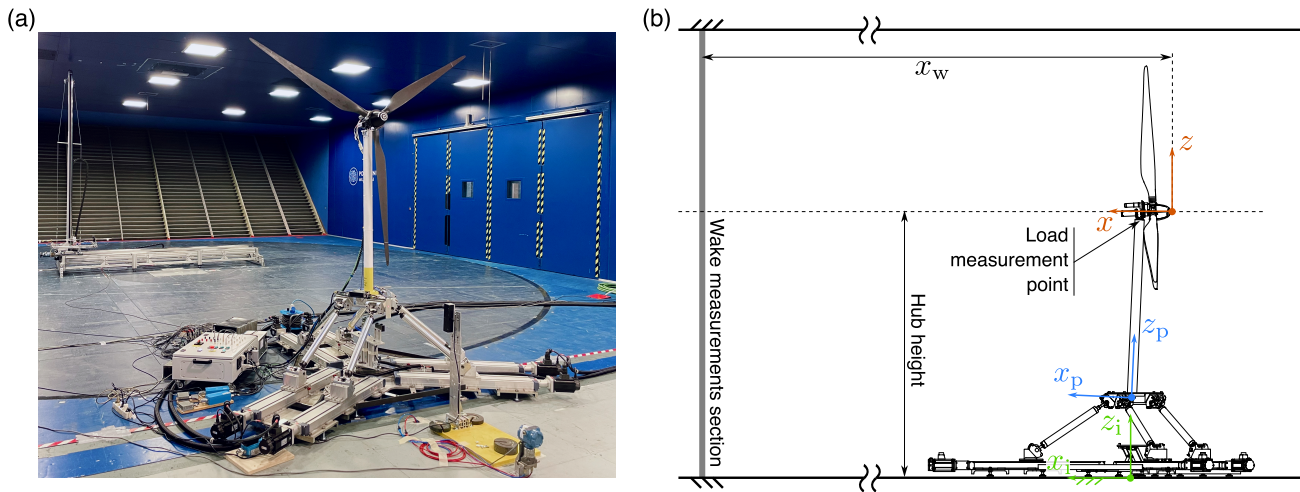

Figure 1. (a): the wind turbine scale model on top of the robotic platform during testing. The traversing system used to measure the wake is visible in the background. **(b)**: schematic representation of the experimental setup with the coordinate systems: $(x_\mathrm{i} - y_\mathrm{i} - z_\mathrm{i})$ is the inertial reference frame, $(x_\mathrm{p} - y_\mathrm{p} - z_\mathrm{p})$ is the platform reference frame, and $(x - y - z)$ is the hub reference frame. x_w is the distance from the wind turbine hub to the section where wake measurements were conducted.

2.1 Wind turbine

The wind turbine is a 1:75 scaled version of the DTU 10-MW (Bak et al., 2013); its geometry is summarized in Table 1. The design of the rotor blades was aimed at mimicking the load distribution of the DTU 10-MW blades, achieving similar thrust and power coefficients. To meet this goal, the wind speed was adjusted by a scale of 1:3 while ensuring the tip-speed-ratio remained the same as that of the full-scale turbine. The blades utilize the low-Reynolds airfoil SD7032, with modified chord and twist to meet the desired thrust force (Bayati et al., 2017b). The rotor thrust determines the wake velocity deficit, and so the chosen scaling approach guarantees that the wake produced by the wind turbine scale model accurately reflects that of a

full-size turbine (Wang et al., 2021). The design of the blades and tower focused on maximizing stiffness to minimize their aeroelastic response.

75   The shaft of the wind turbine had a tilt of $5°$. In tests, the tower was tilted at a negative angle of $5°$ to counteract the wind turbine shaft tilt, ensuring the rotor was vertical to the wind tunnel floor.

Table 1. Geometry of the wind turbine used in the experiment.

Parameter	Unit	Value
Rotor diameter (D)	m	2.381
Blade length	m	1.102
Hub diameter	m	0.178
Hub height	m	2.190
Rotor overhang	m	0.139
Shaft tilt angle	°	5
Tower-to-shaft distance	m	0.064
Tower length	m	1.400
Tower diameter	m	0.075
Tower base offset	m	0.730

2.2   Measurements

Measurements in the test campaign included six-component loads at the tower top, undisturbed wind speed, and wind velocity in the turbine wake. Rotor forces were measured using a six-component force transducer (ATI Mini45 SI-580-20) mounted
80   at the top of the tower. Movements of the robotic platform were recorded with MEL M5L/200 laser sensors and the rotor rotational speed with a magnetic encoder.

The undisturbed wind speed was measured at two locations using Pitot tubes. One tube was positioned 7.5 m ahead of the wind turbine at hub height, while the second was placed at $x_i = 2$ m, $y_i = 5$ m, and $z_i = 3$ m. Substantial agreement was found between the two measurements.

85   The wind velocity in the turbine wake was measured using a hot wire anemometer. A DANTEC 55P11 single-sensor probe with a 5 μm wire diameter, was employed. The wire is perpendicular to the probe's axis, and it is capable of measuring mean and fluctuating velocities of one-dimensional flow. In the wind tunnel campaign, the velocity in the x_i direction, u, was measured. Beyond the wind turbine near wake, this velocity component is predominant over the others. The probe was connected to DISA55M systems operating in constant temperature mode, providing a high dynamic response of up to tens of
90   kHz, making it ideal for turbulence measurements. Prior to testing, the probe was calibrated using a reference nozzle over the expected velocity range.

The measurement uncertainty for the hot wire system was determined using a Monte Carlo simulation, with uncertainties taken into account throughout the entire measurement process, beginning with the probe calibration. Factors contributing to the uncertainty included the accuracy of the data acquisition board and the pressure transducer, which influences both the reference flow velocity during calibration and the upstream wind speed during wind tunnel tests. Additionally, the uncertainty of the thermocouple, which adjusts the hot wire voltage for ambient temperature variations, was considered. The resulting average extended uncertainties, at a 95% confidence level, are $0.17\,\mathrm{m\,s^{-1}}$ for flow speed and 0.4% for turbulence intensity.

The hot wire probe was mounted on an automatic traversing system with two motorized axes, allowing movement in the crosswind $(x_i - y_i - z_i)$ plane. Velocities were measured along lines centered on the rotor hub, both in the horizontal direction (along the y_i-axis) and in the vertical direction (along the z_i-axis). Horizontal measurements were made at 35 evenly spaced points, and vertical measurements at 27 points. The distance between consecutive measurement point is 0.1 m. The traversing system was positioned at three distances downstream of the rotor to study wake evolution: $x_w = [3, 4, 5]D$.

3 Test scenarios

The test scenarios were chosen by revisiting previous studies and considering recent findings in floating wind turbine aerodynamics. While some turbine operating parameters and motion conditions were kept consistent with past research for continuity, other motion cases were selected to induce various excitations in the turbine wake.

All tests were conducted in wind conditions close to laminar, with relatively uniform velocity and turbulence intensity across the wind tunnel section. Prior to testing, wind characteristics were measured and are shown in Fig. 2. The mean velocity over the rotor area varies by 5% compared to the hub mean velocity. Turbulence intensity is 1.5%, reflecting wind conditions that may arise in offshore environments (Türk and Emeis, 2010). Figure 2c displays the power spectral density of wind speed at the wind turbine hub. The air density during testing was $1.185\,\mathrm{kg\,m^{-3}}$.

Every test scenario is defined by the free-stream average wind velocity U_0, the wind turbine rotor speed, the amplitude of platform motion (a), the motion frequency (f), and the oscillation amplitude of the apparent wind speed due to platform displacement (Δu). The motion frequency relates to the free-stream wind through the rotor reduced frequency:

$$f_r = \frac{fD}{U_0}. \tag{1}$$

3.1 Wind conditions and wind turbine settings

The wind turbine was tested at the rated wind speed of $4\,\mathrm{m\,s^{-1}}$, that was also investigated by Fontanella et al. (2021). The wind turbine was operated with a constant rotor speed of 240 rpm, corresponding to the optimal tip-speed ratio of 7.5, and the blade pitch was fixed to $0°$ (i.e., the wind turbine optimal pitch angle).

The wind turbine creates about an 8% geometrical blockage effect, calculated from the rotor area and the wind tunnel test section ratio. This causes the wind speed to rise at the rotor section depending on the turbine's operating conditions. Wind speed at the rotor was measured with the lateral Pitot tube and was consistently $4.2\,\mathrm{m\,s^{-1}}$ in all cases.
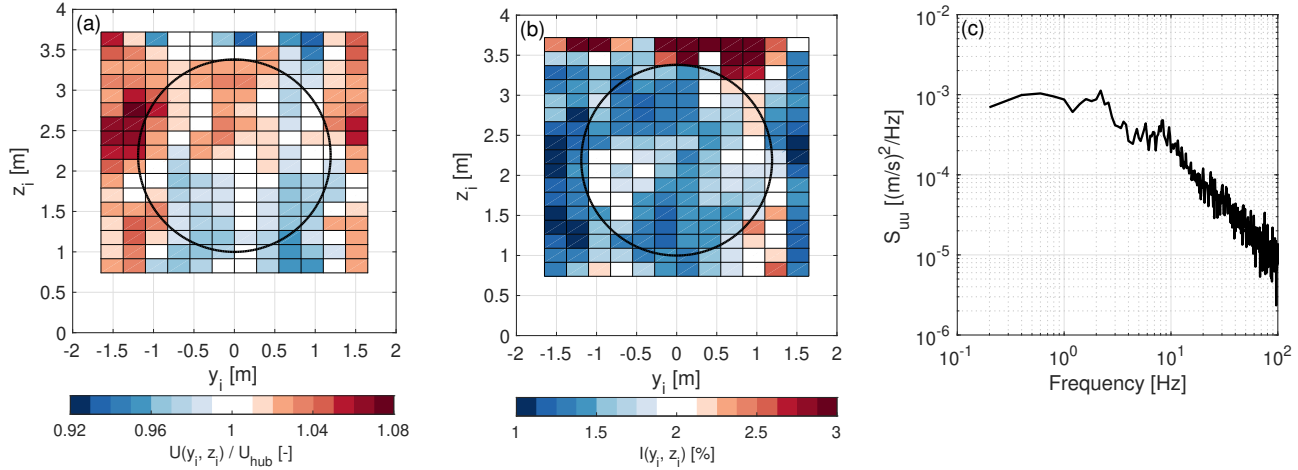
Figure 2. Wind speed at the wind turbine location measured prior to testing. **(a, b)** Normalized mean velocity and turbulence intensity (I) in the wind tunnel test section; the black circle marks the rotor edge. **(c)** Wind velocity power spectral density at the wind turbine hub.

3.2 Platform motion conditions

Platform motions were defined using the inertial reference frame ($x_i - y_i - z_i$) and the platform reference frame ($x_p - y_p - z_p$)

125   that are depicted in Figure 1b. The inertial reference frame has the origin O_i on the wind tunnel floor in correspondence of the tower axis when the robotic platform is at rest; z_i points upward, x_i points in the downwind direction and y_i forms a right-hand backhoe with x_i and z_i. The platform reference frame is fixed to the robotic platform and moves with the turbine; it has the origin O_p in correspondence of the tower base, on the tower centerline; z_p points along the tower axis, x_p points in the downwind direction when the platform is at rest and y_p forms a right-hand backhoe with x_p and z_p. When the wind turbine is

130   in its rest position, the vertical distance between O_p and O_i is $0.73\,\mathrm{m}$.

    The system was studied under harmonic motion of different frequencies and amplitudes. The platform displacement, whether it involves a translation or a rotation, is:

$$d(t) = a \cdot \sin\left(2\pi f t\right). \tag{2}$$

The platform velocity is:

135     $$\dot{d}(t) = a \cdot 2\pi f \cdot \sin\left(2\pi f t\right). \tag{3}$$

    The wind turbine was forced to oscillate in different directions resulting in several motion scenarios that are summarized in Table 2.

Table 2. Test scenarios and wake measurements taken for each of them. Loads were measured in all cases. "H" stands for horizontal and "V" for vertical.

Direction of Platform motion	Amplitude (a) [m] or [°]	Frequency (f) [Hz]	Reduced frequency (f_r) [-]	Δu [m/s]	Measurement section	Measurement direction
Fixed	–	–	–	–	$3D, 4D, 5D$	H, V
Surge	0.032 m	0.5	0.3	0.1	$3D$	H, V
	0.064 m	0.5	0.3	0.2	$3D$	H
	0.016 m	1.0	0.6	0.1	$3D$	H
	0.032 m	1.0	0.6	0.2	$3D, 4D, 5D$	H, V
	0.048 m	1.0	0.6	0.3	$3D$	H
	0.016 m	2.0	1.2	0.2	$3D$	H
	0.032 m	2.0	1.2	0.4	$3D$	H ,V
	0.048 m	2.0	1.2	0.6	$3D$	H
Pitch	1.3°	0.5	0.3	0.1	$3D, 5D$	H, V
	2.5°	0.5	0.3	0.2	$3D$	H, V
	3.0°	0.5	0.3	0.25	$3D$	H, V
	0.6°	1.0	0.6	0.1	$3D$	H, V
	1.3°	1.0	0.6	0.2	$3D, 4D, 5D$	H, V
	1.9°	1.0	0.6	0.3	$3D$	H, V
	0.3°	2.0	1.2	0.1	$3D$	H, V
	0.6°	2.0	1.2	0.2	$3D$	H, V
	1.3°	2.0	1.2	0.4	$3D, 5D$	H, V
	1.9°	2.0	1.2	0.6	$3D$	H, V
Surge–sway 30°	0.032 m	0.5	0.3	0.09	$3D$	H
Surge–sway 15°	0.032 m	1.0	0.6	0.19	$3D$	H
Surge–sway 30°	0.032 m	1.0	0.6	0.17	$3D, 5D$	H
Surge–sway 45°	0.032 m	1.0	0.6	0.14	$3D$	H
Surge–sway 30°	0.032 m	2.0	1.2	0.35	$3D$	H
Roll–pitch 15°	1.3°	1.0	0.6	0.20	$3D$	H
Roll–pitch 30°	1.3°	1.0	0.6	0.18	$3D$	H
Roll–pitch 45°	1.3°	1.0	0.6	0.15	$3D$	H
Yaw	2°	0.5	0.3	–	$3D$	H
	2°	1.0	0.6	–	$3D, 5D$	H
	3°	1.0	0.6	–	$3D$	H
	2°	2.0	1.2	–	$3D$	H

The surge motion corresponds to the translation of O_p along x_i. The pitch motion is a rotation of the platform around the y_i axis, the yaw motion is a rotation of the platform around the z_i axis. Furthermore, the experiment explored platform
140   movements at different angles relative to the wind direction. The surge–sway motion at an angle γ is the combination of a translation $d(t)\cos\gamma$ in the x_i direction and translation $d(t)\sin\gamma$ in the y_i. The rotation of the platform at an angle γ with respect to the wind direction is defined as the combination of a roll rotation around the x_i axis, $d(t)\cos\gamma$, and a pitch rotation, $d(t)\sin\gamma$ around the y_i axis. The yaw motion is a rotation of the platform around the z_i axis.

The rotor experiences an apparent wind when the system undergoes platform motion. The apparent wind velocity results
145   from combining the incoming wind speed (U_0) with the structural velocity of the blades due to platform movement, as shown in Fig. 3.
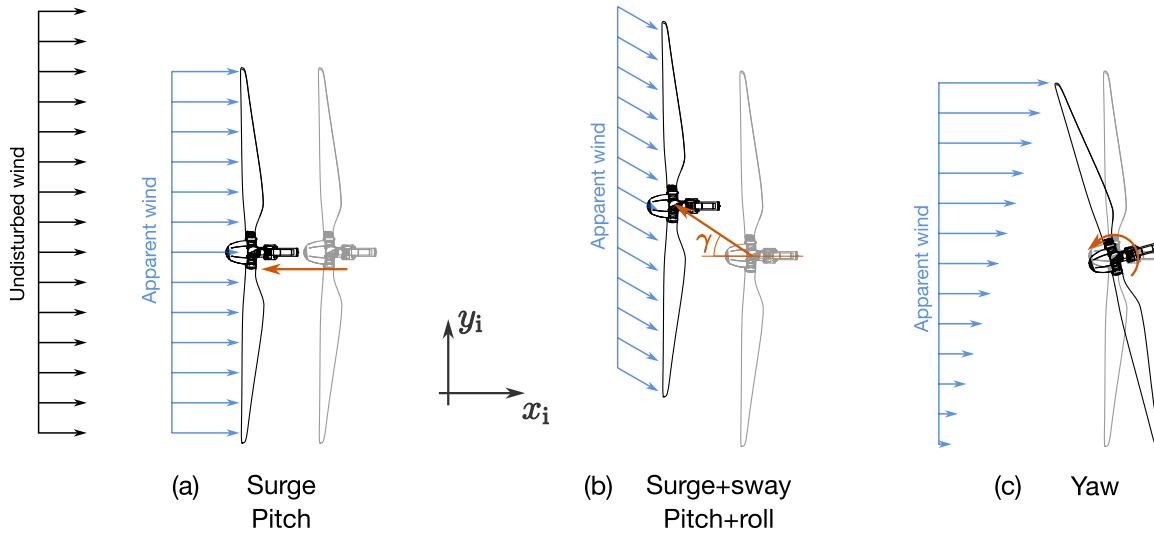
Figure 3. The motion conditions studied in the experiment are classified into three categories: **(a)** surge and pitch motions that cause an apparent wind velocity on the rotor that is aligned to the undisturbed wind; **(b)** motions that combine surge with sway, or pitch with roll, resulting in an apparent wind velocity with a crosswind component; **(c)** yaw movement, resulting in an apparent wind speed gradient across the rotor.

With surge and pitch motions, the rotor is forced to oscillate against the incoming wind. With surge, the blades velocity is equal to the platform velocity and the apparent wind experienced by the rotor is:

$$u_a(t) = U_0 - \dot{d}(t). \tag{4}$$

150   The oscillation amplitude of the apparent wind speed is Δu.

The pitch motion results in a skewed flow due to the rotor plane tilt angle. However, the pitch amplitude is relatively small, and the rotor motion is approximately in the x_i direction; the blades structural velocity is approximated with the hub velocity

in the x_i direction and the apparent wind speed is:

$$u_a(t) = U_0 - \dot{d}_{hub,x}(t), \tag{5}$$

155   with $\dot{d}_{hub,x} = \dot{d}(t) \cdot r_{hub}$, where r_{hub} is the hub distance between O_p and the rotor apex.

When surge and sway or pitch and roll movements combine, they generate a flow with considerable skew. The apparent wind acting on the rotor has components in the x_i and y_i directions. The component in the x_i direction is obtained using Eq. 5, setting $\dot{d}_{hub,x}(t) = \dot{d}(t) \cdot \cos\gamma$ for the surge–sway case and $\dot{d}_{hub,x} = \dot{d}(t) \cdot \cos\gamma \cdot r_{hub}$ for the roll–pitch case. The component in the y_i direction is:

160    $$v_a(t) = -\dot{d}_{hub,y}(t), \tag{6}$$

where $\dot{d}_{hub,y} = \dot{d}(t) \cdot \sin\gamma$ for the surge–sway case and $\dot{d}_{hub,y} = \dot{d}(t) \cdot \sin\gamma \cdot r_{hub}$ for the roll–pitch case.

The velocity of each blade element changes with its radial position during yaw motion. Since the yaw amplitude is small, the blade motion is primarily along the x_i direction. Only this component is considered, and the apparent wind velocity for a blade element is:

165    $$u_a(t) = U_0 - \dot{d}(t) \cdot p_y, \tag{7}$$

where p_y is the distance on the y-axis of the blade element from the rotor apex.

4   Data processing

The tower-top loads were post-processed to obtain the aerodynamic rotor loads. These tower-top loads include forces from rotor aerodynamics and the rotor-nacelle assembly inertia and weight. Inertia and weight contributions were subtracted from
170   the recorded loads using the post-processing method described by Fontanella et al. (2022a), isolating the aerodynamic forces. The aerodynamic loads are represented in the hub reference frame ($x - y - z$).

The aerodynamic rotor loads were analyzed both in the frequency domain and the time domain. The zero-peak amplitude of the aerodynamic loads was computed as the fast Fourier transform (FFT) amplitude at the frequency of platform motion. The phase shift between the aerodynamic rotor load and the platform motion was computed based on the real and imaginary part
175   of the complex FFT at the frequency of interest.

In the time domain, rotor loads exhibit a response at the blade-passing frequency caused by rotor mass imbalance and at higher harmonics resulting from aerodynamic imbalance. The loads were low-pass filtered with a 3 Hz cut-off frequency to eliminate the effects of imbalance. This process was performed in the frequency domain by computing the complex FFT, keeping the frequency components up to 3 Hz, and then utilizing the inverse FFT to reconstruct the signal in the time domain.
180   The filtered loads include approximately 40 periods of platform motion. Subsequently, these loads were binned based on platform motion and phase averaged.

Velocity measurements using a hot wire were taken at a sampling frequency of 10 kHz. To prevent high-frequency electrical noise from skewing the turbulent statistics, the data were digitally filtered with a low-pass filter with a cut-off frequency of

100 Hz. The filter cut-off frequency was chosen carefully after analyzing the turbulent scales to identify the smallest and
highest-frequency energy-containing scales, ensuring accurate estimation of the turbulent kinetic energy. By calculating the
auto-correlation function of the stream-wise velocity at all measurement points, we observed that the smallest and highest-
frequency scales appear in the undisturbed flows approaching the turbine and in the free-stream areas beside the rotor wake. In
these low-turbulence zones, the autocorrelation consistently shows a correlation time of about 0.12 s, suggesting a correlation
scale of around 0.5 m and an integral length scale of around 0.1 m. Filtering at 100 Hz captures the most energetic scales,
along with a significant part of the inertial range of the energy spectrum. Additionally, 100-Hz filtering in free-stream regions
estimated a turbulence intensity of 1.5-2%, aligning with flow measurements conducted before testing (Figure 2). Within the
wake of the wind turbine, the energy-containing scales were observed to be larger in size and lower in frequency, with sufficient
magnitude to dominate electrical noise. Thus, although the filter was not strictly necessary, it was applied consistently across
all regions of the flow.

The acquisition time for each measurement point corresponded to 12 platform motion cycles, allowing to calculate turbulence
statistics over 11 complete platform-motion periods. The velocity time series were binned according to platform motion and
phase-averaged, in a similar manner to the loads.

5 Results

This section presents the findings obtained from a subset of the scenarios introduced in Sect. 3 that was found suitable to
showcase the most interesting phenomena seen in the experiment. Section 5.1 reports the response of aerodynamic rotor loads
to platform motion in different directions. Section 5.2 explores how platform surge and pitch motions influence the wake,
Sect. 5.3 examines the impact of yaw motion, and Sect. 5.4 discusses the effect of crosswind motion from combined surge and
sway.

5.1 Aerodynamic rotor loads

The rotor is perpendicular to the wind tunnel floor and the wind field is uniform in space. When the wind turbine tower base
is fixed, the aerodynamic rotor loads are only the thrust force (F_x) and the torque (M_x), which were equal to $36.47\,\mathrm{N}$ and
$2.97\,\mathrm{N\,m}$, respectively.

Rotor loads oscillate when the wind turbine experiences platform movement. For surge motion, the rotor axis stays aligned
with the wind direction and F_x and M_x are the only aerodynamic loads. Pitch motion and movements resulting from the
combination of surge and sway or pitch and roll, result in a skewed flow. In these cases, there are aerodynamic loads in
different directions ($F_x, F_y, F_z, M_x, M_y, M_z$). However, the amplitude of the loads different from the thrust and torque (i.e.,
F_y, F_z, M_y, M_z) are generally small.

Figure 4 displays the rotor thrust and torque for pitch motion at three different amplitude values, with a frequency of 1 Hz.
The loads are presented over one period of platform motion in the angle domain, using platform-motion phase on the x-axis
instead of time. The average values of M_x match the result with fixed-tower base, F_x in cases with $a = 0.6°$ and $a = 1.9°$ is

slightly lower than in the fixed case; the average F_x in the scenario with $a = 1.3°$ matches that of the fixed-tower base case. The differences in the mean value of F_x are likely due to the zero blade-pitch recalibration done during testing.

F_x and M_x display a sinusoidal pattern at the same motion frequency, with an approximate $90°$ phase shift relative to the platform displacement. This proves that rotor load fluctuations are mainly due to variations in apparent wind speed caused by platform movement (Fontanella et al., 2021).
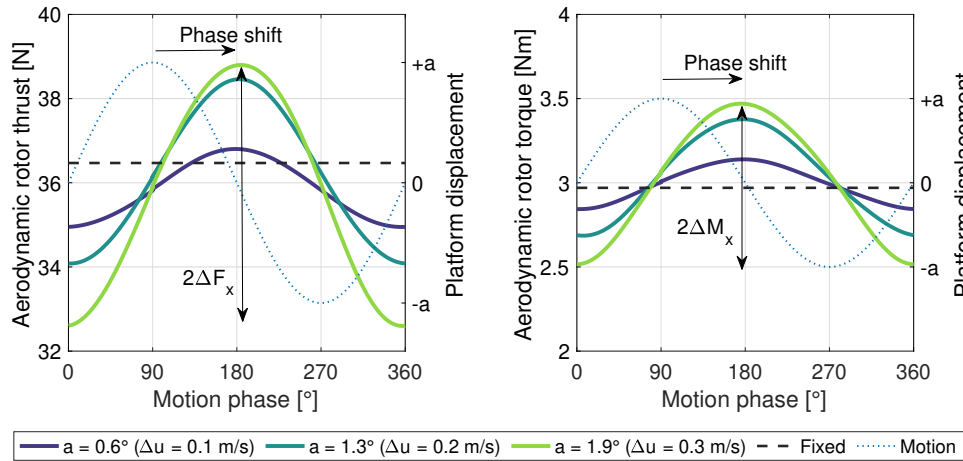
Figure 4. Aerodynamic rotor thrust and torque over one cycle of pitch motion at a frequency of 1 Hz and three different motion amplitudes (a). "Fixed" refers to the scenario with fixed tower base. Δu is the amplitude of apparent wind changes caused by platform motion; ΔF_x and ΔM_x denote the amplitudes of the thrust and torque oscillations, respectively.

To compare loads obtained in the different scenarios involving motions in the surge, sway, roll, and pitch directions, the zero-peak amplitude of thrust and torque, ΔF_x and ΔM_x respectively, were normalized according to the hub motion amplitude in the x_i direction ($d_{hub,x}$) in meters. Figure 5a illustrates the variation in normalized aerodynamic rotor thrust, while Figure 5b presents the variation in normalized aerodynamic rotor torque as the platform motion frequency changes. A linear regression is fitted to the measurements and is included in Figure 5a and Figure 5b. This method of representation demonstrates that the loads change linearly with respect to the platform motion amplitude, as evidenced by the normalized points aligning with the regression line. Additionally, the loads exhibit a linear increase with frequency. The change in rotor aerodynamic loads is linearly proportional to changes in rotor apparent wind along the x_i direction Δu. For example, increasing the amplitude of platform in the x_i direction or the frequency by a factor of 2 would result in changes in rotor aerodynamic loads of the same order. The variation in loads for motion cases at a frequency of 2 Hz exceeds the expected linear trend. For instance, when the surge motion has an amplitude of 0.048 m and a frequency of 2 Hz, the amplitude of thrust force oscillation is 6.99 N and not the 5.6 N predicted by linear regression. This deviation, already seen by Bergua et al. (2023), is attributed to fluctuations in rotor speed and the flexible response of the tower, which could affect the wind turbine behavior under these testing conditions.

Figure 5c and Figure 5d show the phase shift of the aerodynamic rotor loads with respect to the platform motion. The phase
235 shift is approximately $90°$, indicating that the loads oscillations are in phase with the fluctuations in apparent wind speed.
The loads response is consistent with the behavior observed in previous studies investigating platform surge and pitch motions
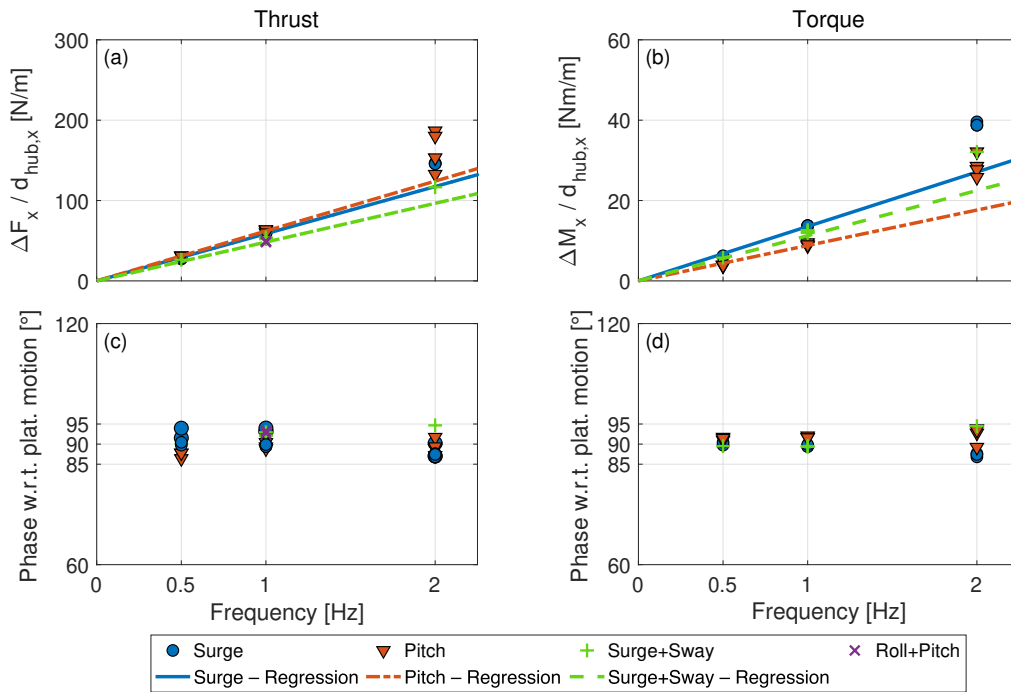(Bergua et al., 2023).

Figure 5. Normalized aerodynamic rotor thrust variation **(a)** and phase shift with respect to platform motion **(c)**. Normalized aerodynamic
rotor torque variation **(b)** and phase shift with respect to platform motion **(d)**.

Yaw motion leads to oscillations in the aerodynamic yaw moment (about the z_p axis). Figure 6 shows the aerodynamic rotor
thrust and the aerodynamic yaw moment in one cycle of yaw motion for four yaw motion scenarios. The yaw moment exhibits
240 a low average value, probably because of a slight misalignment of the wind turbine during the tests. The loads are affected
by oscillations at the frequency of platform motion. These oscillations are determined by the apparent wind speed created by
platform movement u_a, rather than by the misalignment of the rotor relative to the incoming wind, since the yaw angle is
relatively small. Rotor thrust oscillations exhibit much smaller amplitudes compared to those observed in surge, sway, roll,
and pitch motions. In the 0.5 Hz scenario, the oscillations are minimal and almost indistinguishable from measurement noise,
245 resulting in the irregular pattern shown in the figure. Across all four scenarios, the average thrust is marginally lower than that
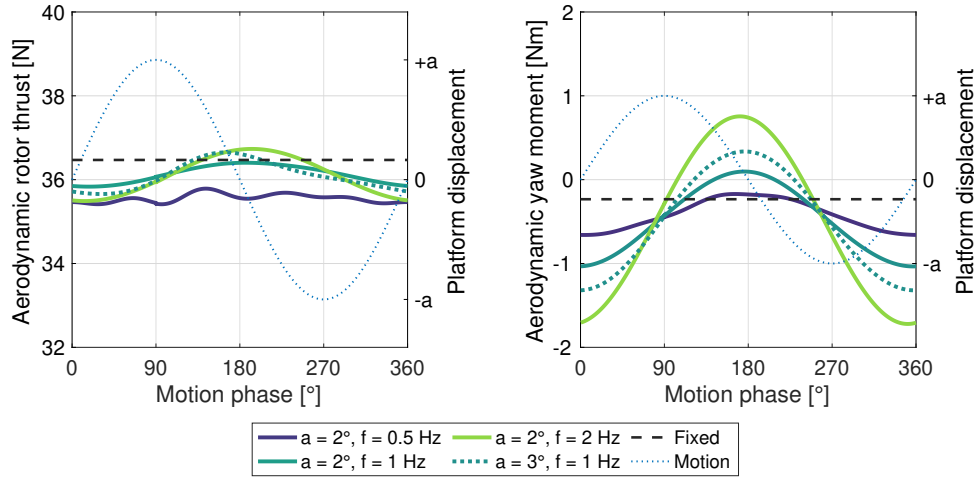of the fixed turbine case.

Figure 6. Aerodynamic rotor thrust and yaw moment (about the z_p axis) over one cycle of yaw motion.

5.2 Wake with platform pitch and surge motions

The analysis of aerodynamic rotor loads indicates that pitch and surge movement leads to periodic thrust changes proportional to apparent wind speed fluctuations caused by the motion.

Figure 7a shows the average velocity profile of the wake at hub height and $x_\mathrm{w} = 3D$, for the wind turbine with a fixed foundation and under four platform pitch motion conditions. The velocity profile has a double-gaussian shape, and it is mostly unaffected by platform motion.

The turbulence intensity in the wake is computed as

$$I(y_\mathrm{i}) = \frac{\sigma_u(y_\mathrm{i})}{U(y_\mathrm{i})}, \tag{8}$$

where $\sigma_u(y_\mathrm{i})$ represents the standard deviation of the local wind speed, while $U(y_\mathrm{i})$ denotes its time-average value. Since $U(y_\mathrm{i})$ is nearly the same in both the platform motion and fixed tower base scenarios, any increase in I is due to greater wind speed variability. The turbulence intensity profiles are reported in Figure 7b. They all show two peaks in correspondence of the rotor edges that are attributed to the wake shear layer. At a platform pitch motion frequency of 1 Hz, the turbulence intensity is increased near the center of the wake, indicating that the mixing layer shifts towards the wake core. This behavior is intensified by increasing the amplitude of motion at a specific frequency (i.e., when the amplitude of the apparent wind speed oscillations experienced by the rotor Δu increases).

Figure 7c examines the velocity at $x_\mathrm{w} = 3D$ and $y_\mathrm{i} = 0.6\,\mathrm{m}$ over one motion cycle. The point at $y_\mathrm{i} = 0.6\,\mathrm{m}$ is selected because it represents half the rotor radius, where the blade undergoes the greatest local normal force variation (Fontanella et al., 2022b), and it does not align with the wake shear layer in the fixed turbine scenario. Significant velocity fluctuations occur at this location when the wind turbine undergoes platform movement, thus $y_\mathrm{i} = 0.6\,\mathrm{m}$ is used for comparing different

motion conditions. The velocity follows a sinusoidal pattern matching the motion frequency. This indicates the presence in the wake of flow structures that are coherent with platform motion.

For the same motion amplitude, the largest velocity oscillations are with $f = 1$ Hz despite this condition having lower thrust variation amplitude (see Figure 5) than at $f = 2$ Hz. When the motion frequency is 2 Hz, oscillations are observed only at the boundaries of the wake (approximately at $y_i \pm 1.1$ m) that corresponds to the location of the shear layer. Coherent flow structures are mostly absent at other locations. As shown in the graph, the sine wave at the motion frequency does not fit the velocity data as well as it does in the 0.5 Hz and 1 Hz cases. Research on dynamic induction control has shown that the evolution of the wake is influenced by the reduced frequency of periodic fluctuations in thrust force (Munters and Meyers, 2018). We assume that similar effects occur in the wake of a floating wind turbine, where fluctuations in thrust force are due to the movement of the platform. Among the conditions explored in this study, the strongest perturbation of the wake occurs when the reduced frequency of platform motion is 0.6. This agrees with the findings of Messmer et al. (2024a) who observed in a wind tunnel experiment that optimal wake recovery occurs with surge motions at a reduced frequency range of 0.5 to 0.8.
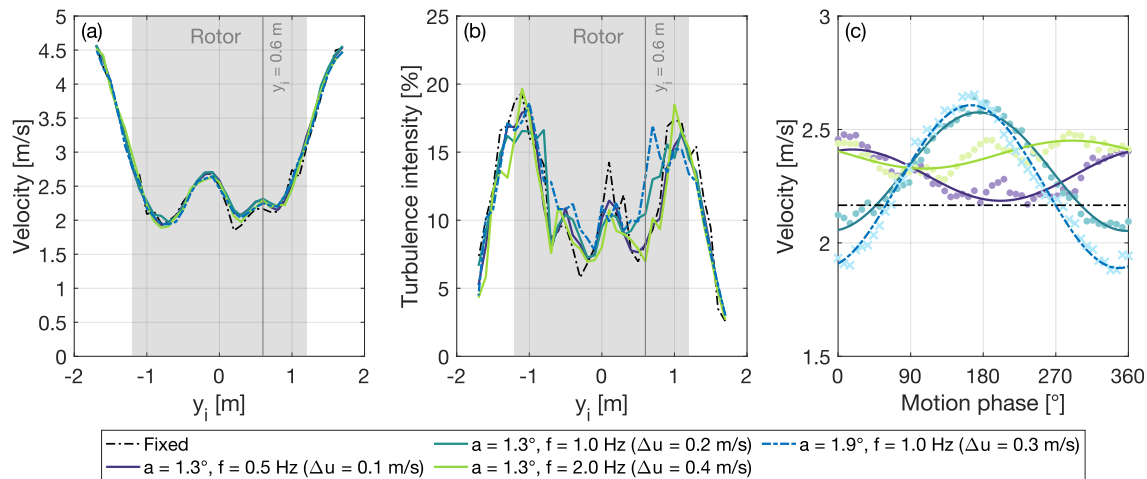

Figure 7. Wake at hub height and $x_w = 3D$ with platform pitch motion. **(a)** Average velocity. **(b)** Turbulence intensity. **(c)** Velocity over one cycle of motion at $y_i = 0.6$ m: the solid lines highlight the first-order sinusoid at the motion frequency.

Velocity fluctuations vary throughout the wake width. This is examined in Fig. 8 that shows the velocity in one cycle of pitch motion at $x_w = 3D$ and various points along the y_i-axis. In general, the amplitude of velocity oscillations and their phase relative to platform motion are not symmetrical with respect to the rotor axis; they vary based on y_i-axis position and motion frequency. The asymmetry might be due to flow in inhomogeneity in the wind tunnel seen in Fig. 2, potentially reducing the correlation between wake flow structures. This hypothesis can be verified through numerical simulations of the experiment, incorporating a high-fidelity model of the wind tunnel inflow.
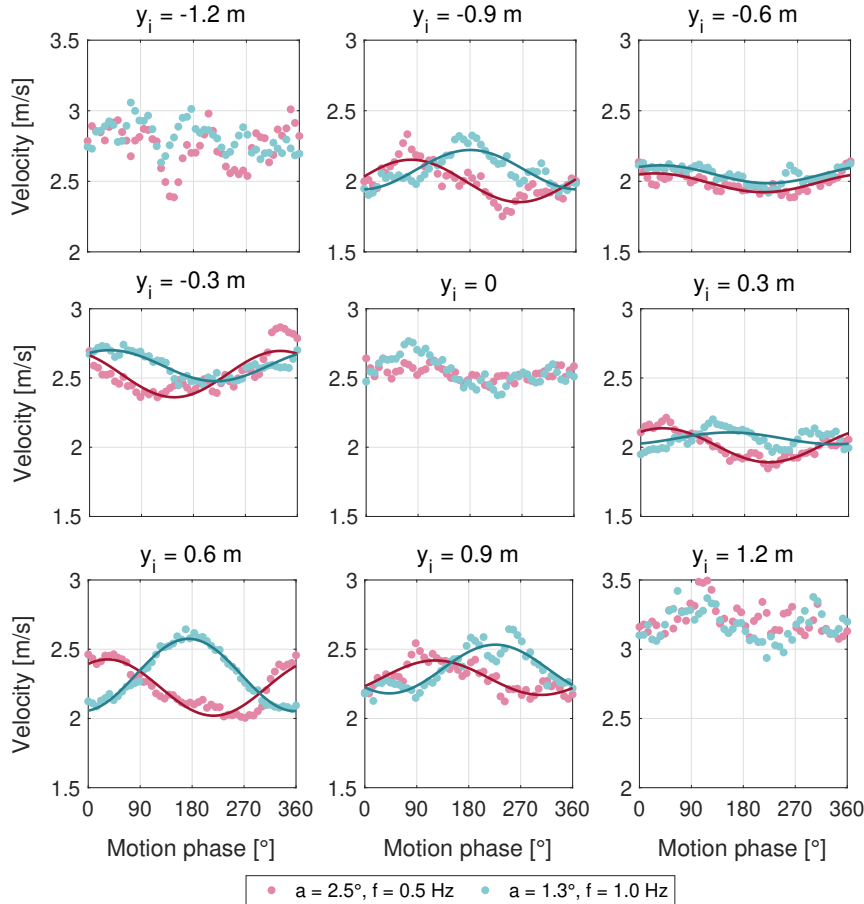
Figure 8. Velocity over one cycle of pitch motion with $\Delta u = 0.2\,\mathrm{m\,s^{-1}}$, $f = 0.5$ Hz and $f = 1$ Hz at $x_\mathrm{i} = 3D$. The solid line highlights the sine wave at the frequency of motion; this is not found in the positions $y_\mathrm{i} = \pm 1.2$ m and $y_\mathrm{i} = 0$.

Figure 9 shows the development of the wake at $x_\mathrm{w} = 5D$. The average velocity exhibits a Gaussian profile that is mostly
285   unchanged by platform motion. The wake velocity in the rotor region (for $|y_\mathrm{i}| \leq 1.2$ m is known at N_p points in the y_i direction that are symmetrically distributed with respect to the x_i-axis; the average velocity in this one-dimensional discrete domain is computed as:

$$U_\mathrm{avg} = \frac{\sum_{j=1}^{N_\mathrm{p}} |r_j| U_j}{\sum_{j=1}^{N_\mathrm{p}} |r_j|}, \qquad (9)$$

where U_j is the time-average velocity at the j-th point which is located at a distance r_j from the x_i-axis. In the rotor region,
290   U_avg with motion is approximately $2.6\,\mathrm{m\,s^{-1}}$, slightly exceeding the average of $2.5\,\mathrm{m\,s^{-1}}$ of the fixed condition.

The turbulence intensity exhibits the two peaks associated with the shear layer, that are situated closer to the wake center than at $x_\mathrm{w} = 3D$. In line with findings at $x_\mathrm{w} = 3D$, the pitch motion scenario at $f = 1$ Hz exhibits higher turbulence at the

15

wake center compared to other scenarios. The shear layer occupies a larger part of the wake compared to the fixed case. The transition from near to far wake appears to be accelerated and is expected to take place closer to the rotor.

295   As shown in Fig. 9c, the coherent flow structures are weaker at $x_{\mathrm{w}} = 5D$ than at $x_{\mathrm{w}} = 3D$. Velocity oscillations of significant amplitude are limited to the wake core and to scenarios with motion at $f = 1$ Hz. We believe that coherent flow structures–larger for $f = 1$ Hz at $3D$ (Fig. 7)–are dissipated as they move downstream by generating small-scale turbulence, which increases the turbulence intensity and accelerates the wake transition.
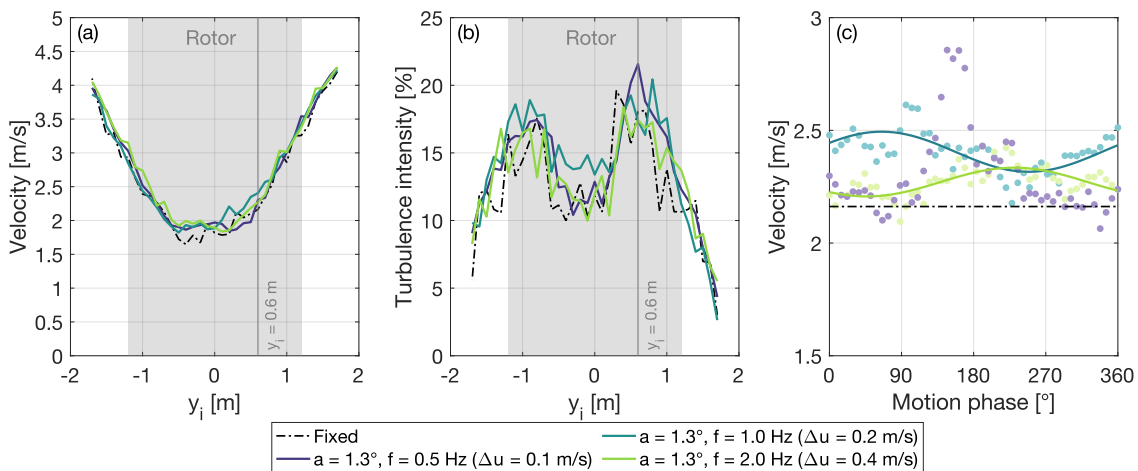
Figure 9. Wake at hub height and $x_{\mathrm{w}} = 5D$ with platform pitch motion. **(a)** Average velocity. **(b)** Turbulence intensity. **(c)** Velocity over one cycle of motion at $y_{\mathrm{i}} = 0.6$ m: the solid lines highlight the first-order sinusoid at the motion frequency.

Figure 10 compares, at $x_{\mathrm{w}} = 3D$, the wake with surge and pitch motions; the two motion conditions are characterized by the

300   same frequency and the same Δu. Their influence on the wake is comparable in terms of average velocity (at $x_{\mathrm{w}} = 5D$, U_{avg} is $2.6 \, \mathrm{m \, s^{-1}}$ in both cases) and turbulence intensity. Motion in the pitch direction causes larger velocity fluctuations, attributed to the small skew of the inflow over the rotor that is absent in surge motion.
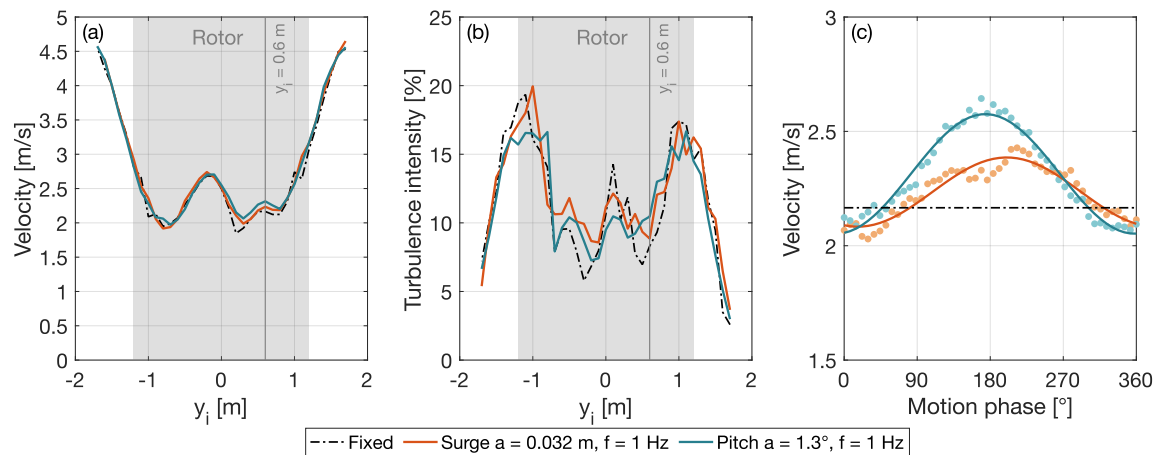
Figure 10. Wake at hub height and $x_w = 3D$ with platform surge and pitch motions. The surge and pitch motions are associated with the same amplitude of apparent wind speed at hub $\Delta u = 0.2\,\mathrm{m\,s^{-1}}$. **(a)** Average velocity. **(b)** Turbulence intensity. **(c)** Velocity at $y_i = 0.6\,\mathrm{m}$ over one cycle of motion.

Figure 11a-b shows the wake along the z_i-axis at $x_w = 3D$ for both surge and pitch motions at $f = 1$ Hz with the same Δu. The velocity over one motion cycle is almost identical, and in pitch the wake center moves only slightly in the vertical direction. Figure 11c compares the average velocity along the z_i-axis at $x_w = 3D$ with different pitch motions. Like the horizontal profile of Figure 7a, the vertical velocity profile exhibits a double-gaussian shape and is largely unaffected by platform movements.
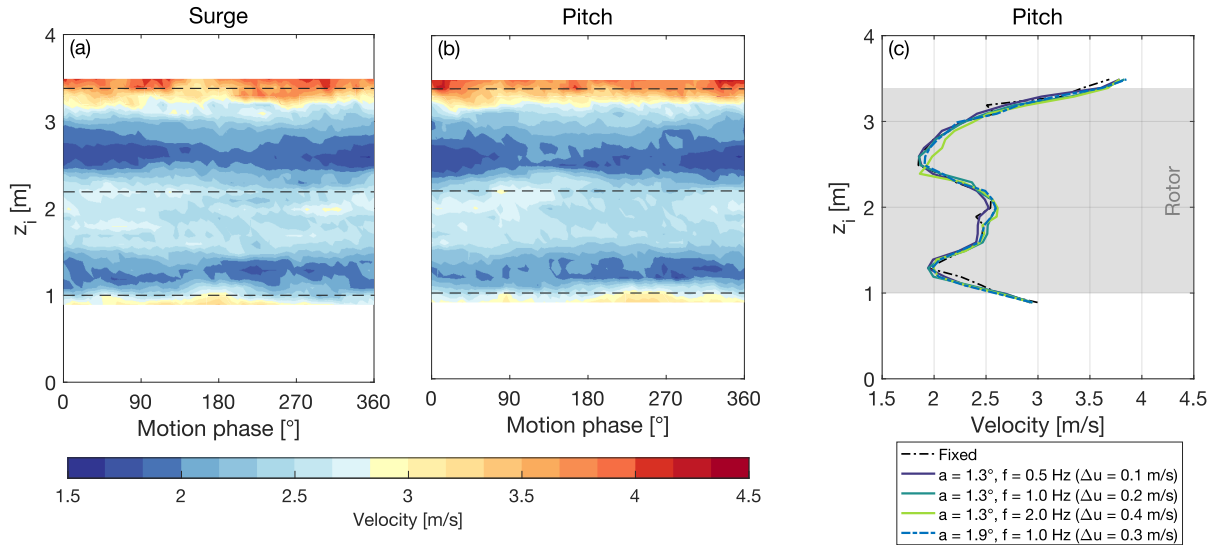
Figure 11. Wake along the z_i-axis and $x_w = 3D$ with platform surge and pitch motions. **(a)** Velocity over one cycle of surge motion with $a = 0.032\,\mathrm{m}$, $f = 1\,\mathrm{Hz}$ (the dashed lines are in correspondence of the rotor axis and the rotor edges). **(b)** Velocity over one cycle of pitch motion with $a = 1.3°$, $f = 1\,\mathrm{Hz}$ (the dashed lines are in correspondence of the rotor axis and the rotor edges). **(c)** Average velocity along the z_i axis with different pitch motions.

5.3 Wake with platform yaw motion

Movement in the yaw direction generates different aerodynamic loads compared to those created by surge or pitch motions. While the thrust variations are minimal, there is an oscillating yaw moment on the rotor. Figure 12 examines the development of

310 the wake at $x_w = 3D$ with platform yaw motion. The average velocity is unchanged compared to the fixed scenario. Turbulence intensity increases near the wake center and decreases close to the rotor edges, showing that the shear layer moves toward the wake center, a pattern also noted with surge and pitch motions. However, this is not the effect of periodic fluctuations in thrust force that are almost absent with movement in the yaw direction (see Fig. 6).

Figure 12c shows the velocity over one cycle of yaw motion with $a = 2°$, $f = 1\,\mathrm{Hz}$. The wake undergoes lateral meandering

315 which is noticeable when tracking the relative maximum at the center and the absolute minimum on the left side of the double-gaussian (black lines in Fig. 12c). The wake lateral movement matches the platform frequency and shows strong correlation across the wake width. We attribute wake meandering to the periodic yaw moment on the rotor. The meandering reaches its peak amplitude when $f = 1\,\mathrm{Hz}$, is reduced when $f = 0.5\,\mathrm{Hz}$, and nearly disappears when $f = 2\,\mathrm{Hz}$. Thus, this wake response is also sensitive to the frequency of the oscillations of the rotor loads and has the highest intensity when f_r is equal to 0.6.

320 At $x_w = 5D$, the meandering disappears. With a yaw motion of $a = 2°$, $f = 1\,\mathrm{Hz}$, U_{avg} is equal to $2.63\,\mathrm{m\,s^{-1}}$ at $x_w = 5D$, showing a 5% increase over the fixed case.
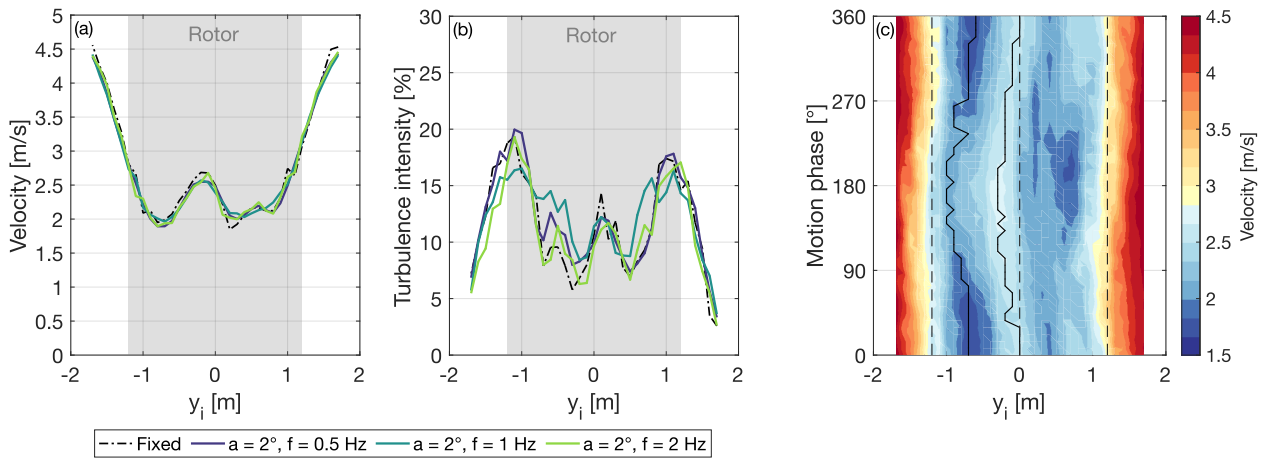
Figure 12. Evolution of the wake at hub height and $x_\mathrm{w} = 3D$ with platform yaw motion. **(a)** Average velocity. **(b)** Turbulence intensity. **(c)** Velocity over one cycle of motion with $a = 2°$, $f = 1$ Hz (the dashed lines are in correspondence of the rotor axis and the rotor edges).

5.4 Wake with platform crosswind motion

Whenever movement in the crosswind direction takes place, thus combining both surge and sway, the apparent wind speed is skewed as depicted in Fig. 3. The thrust exhibits periodic oscillations that are proportional to the rotor forward motion in the x_i direction, similar to those observed in cases of pure surge motion. Additionally, throughout a motion cycle, the wake is released from various positions along the y_i-axis.

Figure 13 shows the wake at $x_\mathrm{w} = 3D$ with motions that are the combination of surge and sway. The platform translation of $a = 0.032\,\mathrm{m}$ and $f = 1$ Hz is at an angle γ ranging from $0°$ (i.e., pure surge motion) to $45°$. When $\gamma = 45°$, the near wake has lateral meandering that is instead absent in the case with $\gamma = 0°$. We attribute wake meandering to the lateral component of the apparent wind v_a at the rotor and to the periodic release of the wake at different y_i positions.

With surge and sway motion, the turbulence intensity in the wake center increases more significantly than with surge motion alone. This increase becomes more pronounced as the angle γ grows, as shown in Fig. 13c. The combination of wake meandering and velocity fluctuations appears to further promote the transition from near to far wake.

At $x_\mathrm{w} = 5D$, the meandering and the velocity fluctuations disappear. With a motion of $a = 0.032\,\mathrm{m}$ and $f = 1$ Hz, with $\gamma = 30°$, the average wake velocity at $x_\mathrm{w} = 5D$ is $2.54\,\mathrm{m\,s^{-1}}$.
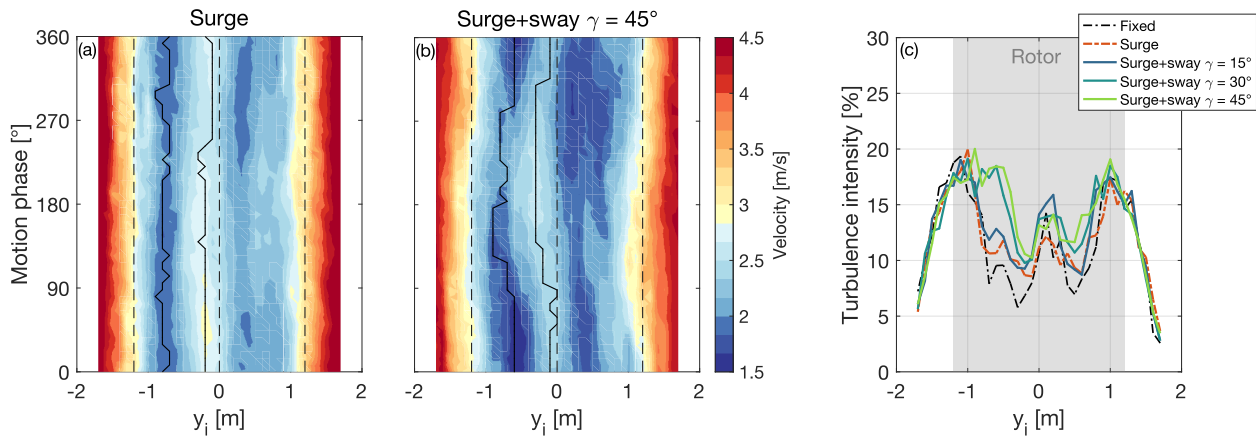
Figure 13. Wake at hub height and $x_i = 3D$ with a platform motion that is the combination of surge and sway. **(a)** Velocity over one cycle of motion with pure surge motion of $a = 0.032\,\mathrm{m}$ and $f = 1$ Hz. **(b)** Velocity over one cycle of motion with a translation motion at angle $\gamma = 45°$ of $a = 0.032\,\mathrm{m}$ and $f = 1$ Hz. **(c)** Turbulence intensity for translation motions with four values of γ (the surge motion corresponds to $\gamma = 0°$).

6 Conclusions

This study investigated how platform motion in different directions affects rotor aerodynamics and correlated the rotor response to wake development. Wake measurements, taken with hot-wire probes from $3D$ to $5D$ downstream, were compared between scenarios with prescribed platform motions and the bottom-fixed case.

340   Depending on the direction of platform motion, we distinguished three conditions. With surge and pitch, the rotor moves in the wind direction; this makes both rotor thrust and torque fluctuate at the same frequency of motion. The oscillations in rotor loads are directly proportional to both the movement amplitude and frequency. The average values of thrust and torque remain relatively unaffected by the platform's motion, indicating that the overall performance of a floating wind turbine is comparable to that of a fixed-bottom turbine. The thrust oscillations translate into fluctuations of the near wake velocity that peak with

345   a motion reduced frequency of 0.6. Yaw motion leads to oscillations of the yaw moment at the rotor and to lateral wake meandering correlated with the platform motion frequency. Combining surge and sway motions results in skewed apparent wind speed, causing lateral wake meandering that adds to the velocity fluctuations caused by oscillations in thrust force. In a floating wind farm, the velocity fluctuations in the wake can lead to fluctuating loads on downstream turbines. Upcoming wind tunnel tests with multiple scale models of floating turbines will investigate this further.

350   The mean velocity within the wake, regardless of the direction of movement, closely matches that of the bottom-fixed scenario. Instead, turbulence intensity increases near the wake center, suggesting a shift of the mixing layer towards the wake core. Increased turbulence is linked to higher wake mixing, which could mean a faster recovery beyond $5D$, the furthest distance examined in the experiment. Future studies should examine the wake further downstream to verify whether the increased wake turbulence induced by motion results in quicker wake recovery.

355 It is understood that greater turbulence intensity in the undisturbed wind facilitates the transition to the far wake by enhancing mixing and helps in recovering the free-stream speed. In offshore environments turbulence intensity depends on the wave height and typically ranges from 3% to 6%. Moreover, vertical wind shear typically happens in the atmospheric boundary layer and is also influenced by sea conditions. This experiment used a 2% turbulence intensity and an almost constant vertical velocity profile. The flow within a wind farm is made even more complex by the interactions between the wakes of various turbines.

360 Future experiments will explore the effects of turbulence and wind shear, as well as the interactions between wakes of floating wind turbines.

All experimental results obtained in this research aim to provide a reliable benchmark to validate numerical tools and to improve their modeling capabilities. Knowledge gained from experiments, along with better simulation tools can be leveraged to optimize future large-scale floating wind farms.

References

375   Bak, C., Zahle, F., Bitsche, R., Kim, T., Yde, A., Henriksen, L., Hansen, M., Blasques, J., Gaunaa, M., and Natarajan, A.: The DTU 10-MW Reference Wind Turbine, danish Wind Power Research 2013 ; Conference date: 27-05-2013 Through 28-05-2013, 2013.

Barter, G. E., Robertson, A., and Musial, W.: A systems engineering vision for floating offshore wind cost optimization, Renewable Energy Focus, 34, 1–16, https://doi.org/https://doi.org/10.1016/j.ref.2020.03.002, https://www.sciencedirect.com/science/article/pii/S1755008420300132, 2020.

380   Bayati, I., Belloli, M., Bernini, L., and Zasso, A.: Wind Tunnel Wake Measurements of Floating Offshore Wind Turbines, vol. 137, pp. 214–222, https://doi.org/10.1016/j.egypro.2017.10.375, https://www.scopus.com/inward/record.uri?eid=2-s2.0-85032015856&doi=10.1016%2fj.egypro.2017.10.375&partnerID=40&md5=aac148722a514dec153f833fee76b361, 2017a.

Bayati, I., Belloli, M., Bernini, L., and Zasso, A.: Aerodynamic design methodology for wind tunnel tests of wind turbine rotors, Journal of
385   Wind Engineering and Industrial Aerodynamics, 167, 217 – 227, https://doi.org/https://doi.org/10.1016/j.jweia.2017.05.004, http://www.sciencedirect.com/science/article/pii/S0167610517301368, 2017b.

Bergua, R., Robertson, A., Jonkman, J., Branlard, E., Fontanella, A., Belloli, M., Schito, P., Zasso, A., Persico, G., Sanvito, A., Amet, E., Brun, C., Campaña Alonso, G., Martín-San-Román, R., Cai, R., Cai, J., Qian, Q., Maoshi, W., Beardsell, A., Pirrung, G., Ramos-García, N., Shi, W., Fu, J., Corniglion, R., Lovera, A., Galván, J., Nygaard, T. A., dos Santos, C. R., Gilbert, P., Joulin, P.-A., Blondel, F., Frickel,
390   E., Chen, P., Hu, Z., Boisard, R., Yilmazlar, K., Croce, A., Harnois, V., Zhang, L., Li, Y., Aristondo, A., Mendikoa Alonso, I., Mancini, S., Boorsma, K., Savenije, F., Marten, D., Soto-Valle, R., Schulz, C. W., Netzband, S., Bianchini, A., Papi, F., Cioni, S., Trubat, P., Alarcon, D., Molins, C., Cormier, M., Brüker, K., Lutz, T., Xiao, Q., Deng, Z., Haudin, F., and Goveas, A.: OC6 project Phase III: validation of the aerodynamic loading on a wind turbine rotor undergoing large motion caused by a floating support structure, Wind Energy Science, 8, 465–485, https://doi.org/10.5194/wes-8-465-2023, https://wes.copernicus.org/articles/8/465/2023/, 2023.

395   Cioni, S., Papi, F., Pagamonci, L., Bianchini, A., Ramos-García, N., Pirrung, G., Corniglion, R., Lovera, A., Galván, J., Boisard, R., Fontanella, A., Schito, P., Zasso, A., Belloli, M., Sanvito, A., Persico, G., Zhang, L., Li, Y., Zhou, Y., Mancini, S., Boorsma, K., Amaral, R., Viré, A., Schulz, C. W., Netzband, S., Soto Valle, R., Marten, D., Martín-San-Román, R., Trubat, P., Molins, C., Bergua, R., Branlard, E., Jonkman, J., and Robertson, A.: On the characteristics of the wake of a wind turbine undergoing large motions caused by a floating structure: an insight based on experiments and multi-fidelity simulations from the OC6 Phase III Project, Wind Energy Science
400   Discussions, 2023, 1–37, https://doi.org/10.5194/wes-2023-21, https://wes.copernicus.org/preprints/wes-2023-21/, 2023.

Fontanella, A., Bayati, I., Mikkelsen, R., Belloli, M., and Zasso, A.: UNAFLOW: a holistic wind tunnel experiment about the aerodynamic response of floating wind turbines under imposed surge motion, Wind Energy Science, 6, 1169–1190, https://doi.org/10.5194/wes-6-1169-2021, https://wes.copernicus.org/articles/6/1169/2021/, 2021.

Fontanella, A., Facchinetti, A., Di Carlo, S., and Belloli, M.: Wind tunnel investigation of the aerodynamic response of two 15 MW floating
405   wind turbines, Wind Energy Science, 7, 1711–1729, https://doi.org/10.5194/wes-7-1711-2022, https://wes.copernicus.org/articles/7/1711/2022/, 2022a.

Fontanella, A., Zasso, A., and Belloli, M.: Wind tunnel investigation of the wake-flow response for a floating turbine subjected to surge motion, Journal of Physics: Conference Series, 2265, 042 023, https://doi.org/10.1088/1742-6596/2265/4/042023, https://dx.doi.org/10.1088/1742-6596/2265/4/042023, 2022b.

410   Messmer, T., Hölling, M., and Peinke, J.: Enhanced recovery caused by nonlinear dynamics in the wake of a floating offshore wind turbine, Journal of Fluid Mechanics, 984, A66, https://doi.org/10.1017/jfm.2024.175, 2024a.

Messmer, T., Peinke, J., and Hölling, M.: Wind tunnel investigation on the recovery and dynamics of the wake of a floating offshore wind turbine subjected to low inflow turbulence, Journal of Physics: Conference Series, 2767, 092 083, https://doi.org/10.1088/1742-6596/2767/9/092083, https://dx.doi.org/10.1088/1742-6596/2767/9/092083, 2024b.

415 Meyers, J., Bottasso, C., Dykes, K., Fleming, P., Gebraad, P., Giebel, G., Göçmen, T., and van Wingerden, J.-W.: Wind farm flow control: prospects and challenges, Wind Energy Science, 7, 2271–2306, https://doi.org/10.5194/wes-7-2271-2022, https://wes.copernicus.org/articles/7/2271/2022/, 2022.

Munters, W. and Meyers, J.: Towards practical dynamic induction control of wind farms: analysis of optimally controlled wind-farm boundary layers and sinusoidal induction control of first-row turbines, Wind Energy Science, 3, 409–425, https://doi.org/10.5194/wes-3-409-2018, 420 https://wes.copernicus.org/articles/3/409/2018/, 2018.

Nettuno: NETTUNO, https://www.nettuno-project.it, accessed: 22/10/2024, 2023.

Özinan, U., Gräfe, M., Schulz, C. W., and Cheng, P. W.: Near-wake measurements and simulations of a floating wind turbine using a four-beam nacelle-based lidar, Journal of Physics: Conference Series, 2767, 092 100, https://doi.org/10.1088/1742-6596/2767/9/092100, https://dx.doi.org/10.1088/1742-6596/2767/9/092100, 2024.

425 Schliffke, B., Aubrun, S., and Conan, B.: Wind Tunnel Study of a "Floating" Wind Turbine's Wake in an Atmospheric Boundary Layer with Imposed Characteristic Surge Motion, Journal of Physics: Conference Series, 1618, 062 015, https://doi.org/10.1088/1742-6596/1618/6/062015, https://doi.org/10.1088%2F1742-6596%2F1618%2F6%2F062015, 2020.

Schliffke, B., Conan, B., and Aubrun, S.: Floating wind turbine motion signature in the far-wake spectral content – a wind tunnel experiment, Wind Energy Science, 9, 519–532, https://doi.org/10.5194/wes-9-519-2024, https://wes.copernicus.org/articles/9/519/2024/, 2024.

430 Türk, M. and Emeis, S.: The dependence of offshore turbulence intensity on wind speed, Journal of Wind Engineering and Industrial Aerodynamics, 98, 466–471, https://doi.org/https://doi.org/10.1016/j.jweia.2010.02.005, https://www.sciencedirect.com/science/article/pii/S0167610510000279, 2010.

Wang, C., Campagnolo, F., Canet, H., Barreiro, D. J., and Bottasso, C. L.: How realistic are the wakes of scaled wind turbine models?, Wind Energy Science, 6, 961–981, https://doi.org/10.5194/wes-6-961-2021, https://wes.copernicus.org/articles/6/961/2021/, 2021.